

USING *CHANDRA* TO UNVEIL THE HIGH-ENERGY PROPERTIES OF THE HIGH MAGNETIC FIELD RADIO PULSAR J1119–6127

SAMAR SAFI-HARB^{1,2} AND HARSHA S. KUMAR¹

Received 2007 October 1; accepted 2008 May 23

ABSTRACT

PSR J1119–6127 is a high magnetic field ($B = 4.1 \times 10^{13}$ G), young (≤ 1700 year old), and slow ($P = 408$ ms) radio pulsar associated with the supernova remnant (SNR) G292.2–0.5. In 2003, *Chandra* allowed the detection of the X-ray counterpart of the radio pulsar and provided the first evidence for a compact and faint pulsar wind nebula (PWN). We here present new *Chandra* observations that allowed for the first time an imaging and spectroscopic study of the pulsar and PWN independently of each other. The PWN is only evident in the hard band (above ~ 2 keV) and consists of jetlike structures extending at least $7''$ from the pulsar, with the southern “jet” being longer than the northern “jet.” The spectrum of the PWN is described by a power law with a photon index $\Gamma \sim 1.1$ for the compact PWN and ~ 1.4 for the southern long jet (at a column density $N_H = 1.8 \times 10^{22}$ cm^{–2}), and a total luminosity $L_X(0.5–7.0$ keV) $\sim 4 \times 10^{32}$ ergs s^{–1}, at a distance of 8.4 kpc. We rule out a single blackbody model for the pulsar and present the first evidence of nonthermal emission that dominates above ~ 3 keV. A two-component model consisting of a power-law component (with photon index $\Gamma \sim 1.5–2.0$) plus a thermal component provides the best fit. The thermal component can be fit by either a blackbody model with a temperature $kT \sim 0.21$ keV, or a neutron star atmospheric model with a temperature $kT \sim 0.14$ keV. The efficiency of the pulsar in converting its rotational power, \dot{E} , into nonthermal X-ray emission from the pulsar and PWN is $\approx 5 \times 10^{-4}$, comparable to other rotation-powered pulsars with a similar \dot{E} . We discuss our results in the context of the X-ray manifestation of high magnetic field radio pulsars in comparison with rotation-powered pulsars and magnetars.

Subject headings: ISM: individual (G292.2–0.5) — pulsars: individual (PSR J1119–6127) — supernova remnants — X-rays: ISM

1. INTRODUCTION

A pulsar wind nebula (PWN) is a bubble of relativistic particles and magnetic field, powered by the rotational energy of a young energetic pulsar. The PWN’s nonthermal emission arises from synchrotron radiation of the high-energy particles injected by the pulsar and accelerated at the site where the relativistic pulsar wind is decelerated by the confining medium. As such, PWNs represent an ideal laboratory to study the physics of neutron stars, particle acceleration, and relativistic shocks.

The Crab nebula has been viewed for almost three decades as the canonical example of how a fast rotation-powered pulsar dumps its energy into its surroundings. However, the past several years have witnessed a synergy of high-energy observations pointing to a growing class of compact objects that manifest themselves differently from the Crab. These include the anomalous X-ray pulsars (AXPs) and the soft gamma-ray repeaters (SGRs), commonly believed to be highly magnetized neutron stars, or magnetars ($B \sim 10^{14}–10^{15}$ G), powered by magnetic field decay rather than by rotation, and characterized by relatively slow periods (5–12 s; see Woods and Thompson 2006 for a review). So far, there is no evidence of PWNs surrounding these objects. Furthermore, they were believed to be radio-quiet. However, recently radio emission has been observed from the transient magnetar XTE J1810–197 (Halpern et al. 2005; Camilo et al. 2006), and 2 s radio pulsations have been discovered from a new magnetar (1E 1547.0–5408; Camilo et al. 2007).

Interestingly, there are about half a dozen radio pulsars with spin and magnetic field properties intermediate between the “clas-

sical” Crab-like pulsars³ and the magnetars; their spin periods range from a fraction of a second to ~ 7 s, and their magnetic field⁴ is close to the QED value of 4.4×10^{13} G (the field at which the electron’s rest mass energy equals its cyclotron energy). The question whether these pulsars should display more magnetar-like or Crab-like properties is still under debate (see, e.g., the references in Table 3). X-ray observations targeted to study these objects offer the best window to address this question and better understand their emission properties. The search for and study of any associated PWN should, in particular, shed light on the nature of their high-energy emission in comparison with the other pulsars.

PSR J1119–6127 is a member of this small, yet growing, class of objects. It was discovered in the Parkes multibeam pulsar survey (Camilo et al. 2000). It has a rotation period P of 408 ms, a large period derivative \dot{P} of 4×10^{-12} , a characteristic age $P/2\dot{P}$ of 1600 yr, a surface dipole magnetic field B of 4.1×10^{13} G, a spin-down luminosity \dot{E} of 2.3×10^{36} ergs s^{–1}, and a braking index of 2.9, implying an upper limit on its age of 1700 years (under standard assumptions of simple spin-down). No radio PWN was detected around the pulsar despite its youth (Crawford et al. 2001). The pulsar was found within the supernova remnant (SNR) G292.2–0.5 of $15'$ in diameter, discovered with the Australia Telescope Compact Array (ATCA; Crawford et al. 2001) and subsequently detected with X-ray observations acquired with the *ROSAT* satellite and the *Advanced Satellite for Cosmology and Astrophysics* (*ASCA*; Pivovarov et al. 2001).

The X-ray counterpart to the radio pulsar was first resolved with *Chandra*, which also revealed for the first time evidence of

¹ Physics and Astronomy Department, University of Manitoba, Winnipeg, MB R3T 2N2, Canada.

² Canada Research Chair; samar@physics.umanitoba.ca.

³ A Crab-like pulsar here refers to a rotation-powered pulsar powering a PWN.

⁴ The magnetic field is derived assuming magnetic dipole radiation and is related to the spin period, P , and the spin-down period derivative, \dot{P} , as $B = 3.2 \times 10^{19} (P\dot{P})^{1/2}$ G.

a compact ($3'' \times 6''$) PWN (Gonzalez & Safi-Harb 2003, hereafter GSH03). The pulsar was subsequently detected with *XMM-Newton* and was found to exhibit thermal emission with an unusually high pulsed fraction of $74\% \pm 14\%$ in the 0.5–2.0 keV range (Gonzalez et al. 2005). The *XMM-Newton*–derived temperature was also unusually high, in comparison with other pulsars of similar age or even younger, like the pulsar in the SNR 3C 58 (Slane et al. 2002).

While a spectrum of the pulsar has been obtained with the previous *Chandra* and *XMM-Newton* observations, the *Chandra* spectrum suffered from poor statistics, and it was not possible to extract a spectrum from the PWN. The *XMM-Newton* spectrum of the pulsar was contaminated by the PWN’s spectrum due to the large point-spread function (PSF) of *XMM-Newton*.

In this paper, we present new observations of the pulsar obtained with *Chandra* and targeted to constrain the properties of the pulsar and associated PWN. In a follow-up paper, we present the study of the associated SNR, to complement the previous study of the western side of the remnant by Gonzalez & Safi-Harb (2005).

The distance to the pulsar was determined to be in the 2.4–8.0 kpc range (Camilo et al. 2000). Using the fitted X-ray column density to the pulsar and that to its associated SNR, GSH03 estimated a distance in the 4.0–12.6 kpc range, but the location of the source with respect to the Carina spiral arm (Camilo et al. 2000) puts an upper limit on the distance of ~ 8 kpc. The Cordes-Lazio Galactic free electron density model (NE2001; Cordes & Lazio 2002) suggests a much larger distance of 16.7 kpc, while Caswell et al. (2004) estimate a distance of 8.4 kpc using neutral hydrogen absorption measurements to the SNR. In this work, we adopt the distance to the SNR of 8.4 kpc and scale all derived quantities in units of $d_{8.4} = D/8.4$ kpc.

The paper is organized as follows. In § 2, we summarize the *Chandra* observations. In §§ 3 and 4, we present our imaging and spectroscopic results, respectively. Finally, in § 5 we present our discussion and conclusions.

2. OBSERVATIONS AND DATA ANALYSIS

PSR J1119–6127 was observed with *Chandra* in cycle 5 on 2004 November 2–3 (ObsID 6153) and October 31–November 1 (ObsID 4676). We combine these new data with the observation conducted during cycle 3 (ObsID 2833; GSH03) in order to improve on the statistics. All three observations were positioned at the aimpoint of the back-illuminated S3 chip of the Advanced CCD Imaging Spectrometer (ACIS). X-ray photon events were acquired in the timed-exposure readouts, at a CCD temperature of -120°C and a frame readout time of 3.2 s, and telemetered to the ground in the “Very Faint” mode. The roll angles were chosen such that the AO-3 data covered the western side of the SNR and the AO-5 data covered the eastern side (see Fig. 1). The data were then reduced using standard CIAO version 4.0 routines.⁵ We have created a cleaned events file by retaining events with the standard *ASCA* grades 02346 and rejecting hot pixels. In addition, the data were filtered for good time intervals, removing periods with high background rates or unstable aspect. The resulting effective exposure time was 56.8 ks for ObsID 2833, 60.5 ks for ObsID 4676, and 18.9 ks for ObsID 6153, yielding a total effective exposure time for the three combined observations covering the field around the pulsar of 136.2 ks.

3. IMAGING RESULTS

3.1. G292.2-0.5

Figure 1 shows the *Chandra* cycle 3 (covering the western side of the remnant) and cycle 5 (covering the eastern side of the

remnant) observations overlaid on the *ASCA* hard band (2–10 keV) image, with the radio extent of the SNR shown as a black circle overlaid. The central circle denotes the position of the pulsar. The image illustrates the power of *Chandra* in resolving the X-ray emission and shows the overlap between the *Chandra* observations, leading to a deep exposure of the pulsar and central regions of the SNR. The pulsar and surrounding region will be the focus of this paper. The properties of the diffuse emission from the SNR will be presented in a separate paper.

Figure 2 shows the combined *Chandra* tricolor image, zoomed on the pulsar region, and obtained as follows: The data were first divided into individual images in the soft (0.5–1.15 keV, red), medium (1.15–2.3 keV, green), and hard (2.3–10.0 keV, blue) bands (the energy boundaries were chosen to match those in GSH03). Individual background images were then obtained from the blank-sky data sets available in CIAO. For each observation, background images were reprojected to match the corresponding events file. The background images were then divided into the same energy bands mentioned above, and then subtracted from their corresponding source+background image. The resulting images were subsequently adaptively smoothed⁶ using a Gaussian with $\sigma = 1''$ for significance of detection >5 and up to $\sigma = 5''$ for significance down to 2. The individual background-subtracted images were then combined to produce the image shown in Figure 2. As in our previous X-ray study (GSH03), the X-ray emission can be resolved into several X-ray sources (tabulated in Gonzalez & Safi-Harb 2005, Table 2), surrounded by diffuse emission from the SNR interior. In addition, the pulsar and associated PWN immediately stand out as a hard (blue) source.

3.2. PSR J1119–6127 and Its PWN

The peak of the X-ray emission from the pulsar is positioned at $\alpha_{J2000.0} = 11^{\text{h}}19^{\text{m}}14.26^{\text{s}}$, $\delta_{J2000.0} = -61^\circ27'49.3''$, which match within error the radio coordinates of the pulsar $\alpha_{J2000.0} = 11^{\text{h}}19^{\text{m}}14.3^{\text{s}}$ and $\delta_{J2000.0} = -61^\circ27'49.5''$ (with $0.3''$ error).

In order to compare the source’s spatial characteristics with *Chandra*’s PSF, we performed a two-dimensional spatial fit to the new *Chandra* data using the SHERPA software.⁷ We created images of the source in the soft (0.5–1.15 keV), medium (1.15–2.3 keV), and hard (2.3–10 keV) bands. We subsequently created normalized PSF images at the energies characteristic of the source’s energy histogram. These images were then used as convolution kernels when fitting. The soft band image yielded a FWHM value of $0.8''$ consistent with a point source, the medium band image gave a slightly higher value of $0.9''$, while the hard band was best described by an elliptical Gaussian function with FWHM $0.9'' \times 1.2''$, confirming the extended nature of the PWN in the hard band, a result that is consistent with GSH03.

In Figures 3 and 4, we show zoomed-in images of the PWN. Figure 3 shows the raw soft band (0.5–2 keV) and hard band (2–10 keV) images centered on the pulsar, and Figure 4 shows the same images adaptively smoothed using a Gaussian with $\sigma = 1''$ for a significance of detection greater than 5 and up to $\sigma = 3''$ for a significance of detection down to 2. As mentioned earlier, the PWN structures (further discussed below) are also visible using a simple Gaussian smoothing. We verified that they are also evident in the hard band images for the individual observations.

⁶ The “csmooth” CIAO tool is based on the “asmooth” algorithm (Ebeling et al. 2006), which has the advantage of visually enhancing extended features in noise-dominated regions. We note that the compact PWN and the southern jet display a similar morphology using a simple Gaussian smoothing.

⁷ See <http://cxc.harvard.edu/sherpa/>.

⁵ See <http://cxc.harvard.edu/ciao/>.

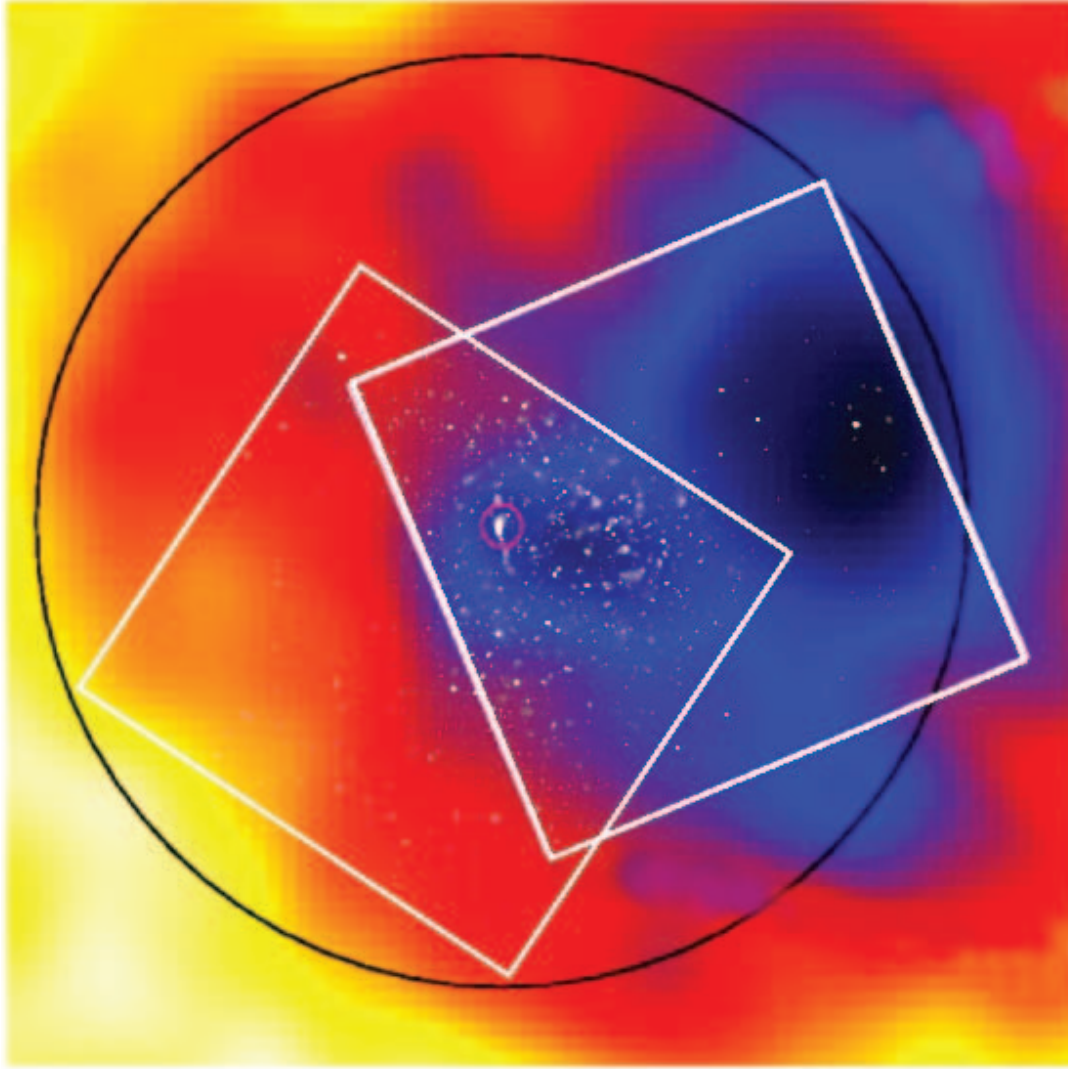


FIG. 1.—The 2.0–10.0 keV *ASCA* image of SNR G292.2–0.5, smoothed with a Gaussian with $\sigma = 45''$, with the black circle showing the radio boundary ($15'$ in diameter). The superposed squares mark the locations of the $8' \times 8'$ *Chandra*'s S3 chip during AO-3 (right) and AO-5 (left), covering the western and eastern sides of the remnant, respectively, with the gray-scale image showing the raw 0.5–10 keV emission seen with *Chandra*. The central circle marks the position of PSR J1119–6127. North is up and east is to the left.

Furthermore, using the *celldetect* CIAO routine, we did not find any point sources within the PWN, thus ruling out the contamination of the PWN structures by background sources.

The images clearly show that the PWN is harder than the pulsar and can be resolved into elongated “jetlike” structures extending at least $7''$ north and south of the pulsar. This confirms the evidence of a hard PWN associated with this high magnetic field pulsar (GSH03) but also shows that the PWN is larger than originally thought. The PWN is elongated in the north-south direction, with the northern extension (which we refer to as a jet) appearing tilted to $\sim 30^\circ$ west of north, and the southern jet being more elongated and ~ 2 times brighter than the northern jet. In Figure 5 we highlight the first evidence for a more extended ($\gtrsim 20''$) faint and hard jetlike structure southwest of the pulsar.

We accumulate 100 ± 23 background-subtracted source counts from this region, which on top of 99 ± 21 background counts (normalized to the source area), imply a $\sim 7 \pm 2 \sigma$ detection (0.5–7.0 keV). It is not clear whether this structure is an extension of the southern compact jet seen closer to the pulsar or an SNR filament. However, its morphology (in particular its knotty structure that is similar to Vela’s long jet; Kargaltsev et al. 2003) and spectrum (see § 4.2)

suggest an association with PSR J1119–6127’s PWN, a result that can be confirmed with a deeper exposure. We note that while the *XMM-Newton* MOS2 image shows a hint of a southern extension, the large and distorted PSF of the MOS2 camera does not allow a confirmation of this jet (M. Gonzalez 2008, private communication).

In the following, we refer to the PWN region shown in the right panel of Figure 4, (size $\sim 6''$ in the east-west direction by $\sim 15''$ in the north-south direction) as the “compact PWN,” and to the extended jetlike structure southwest of the pulsar (size $\sim 6'' \times 20''$; see Fig. 5) as the southern jet. We note here that it is possible that the compact PWN corresponds to a torus viewed edge-on. However, the southern extension (if proven to be a jet associated with the pulsar) would falsify this interpretation as the jets are expected to be perpendicular to the torus. We further discuss these features in §§ 4.2 and 5.2.

4. SPATIALLY RESOLVED SPECTROSCOPY

The spectral analysis was performed using the X-ray spectral fitting package, XSPEC version 12.4.0,⁸ and constrained to the

⁸ See <http://xspec.gsfc.nasa.gov>.

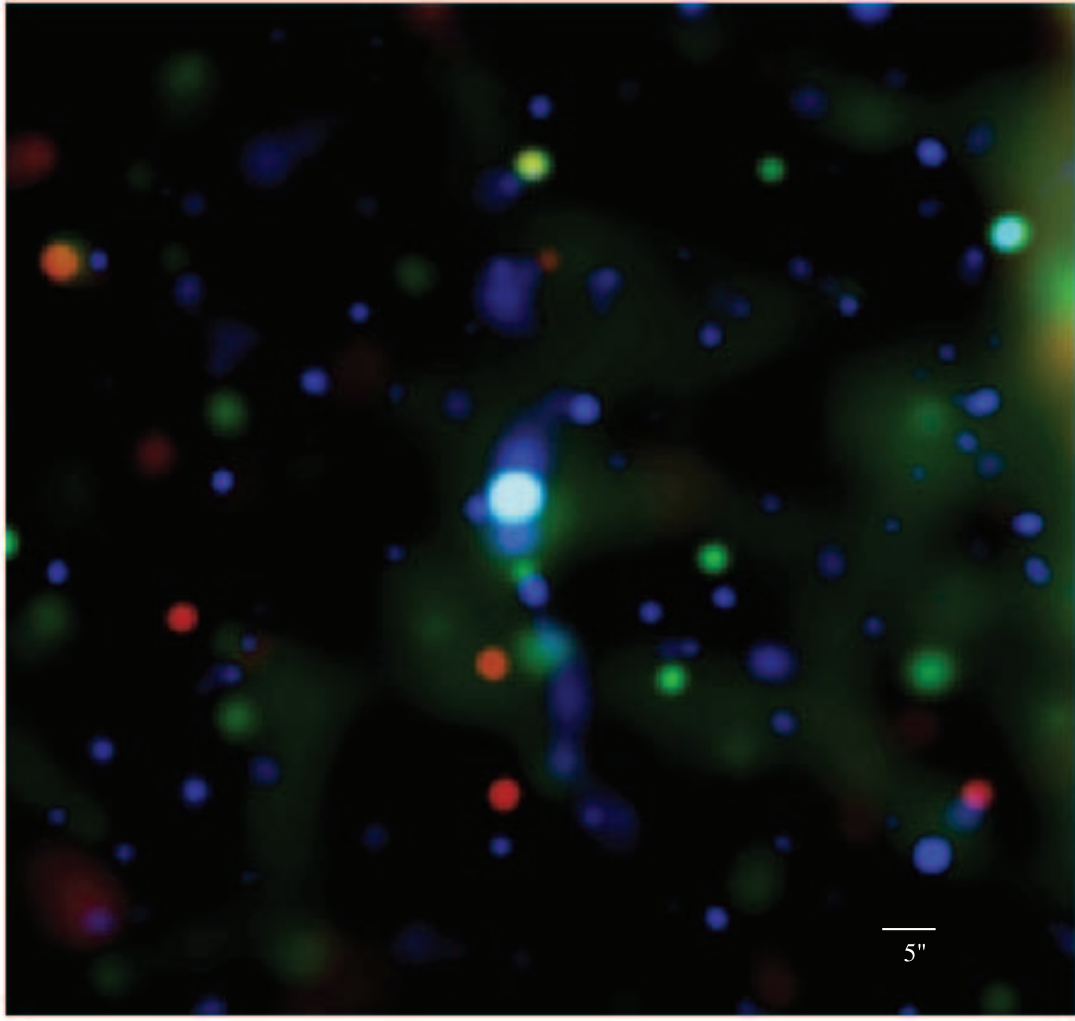


FIG. 2.— Tricolor energy image of PSR J1119–6127 and associated PWN. The image is $2.4' \times 2.3'$ in size and is exposure-corrected. Red, green, and blue correspond to 0.5–1.15, 1.15–2.3, and 2.3–10.0 keV, respectively (see § 3.1 for details).

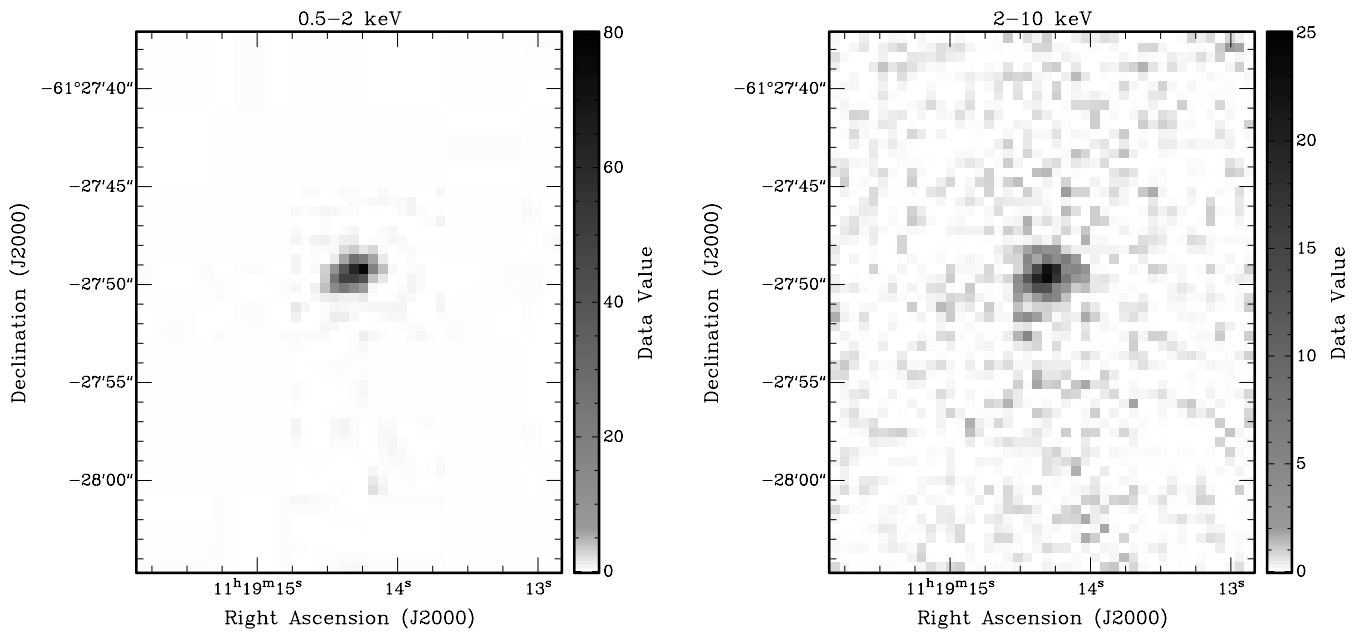


FIG. 3.— Raw soft (0.5–2.0 keV) and hard (2.0–10 keV) images of PSR J1119–6127 and associated nebula. These images were not background-subtracted.

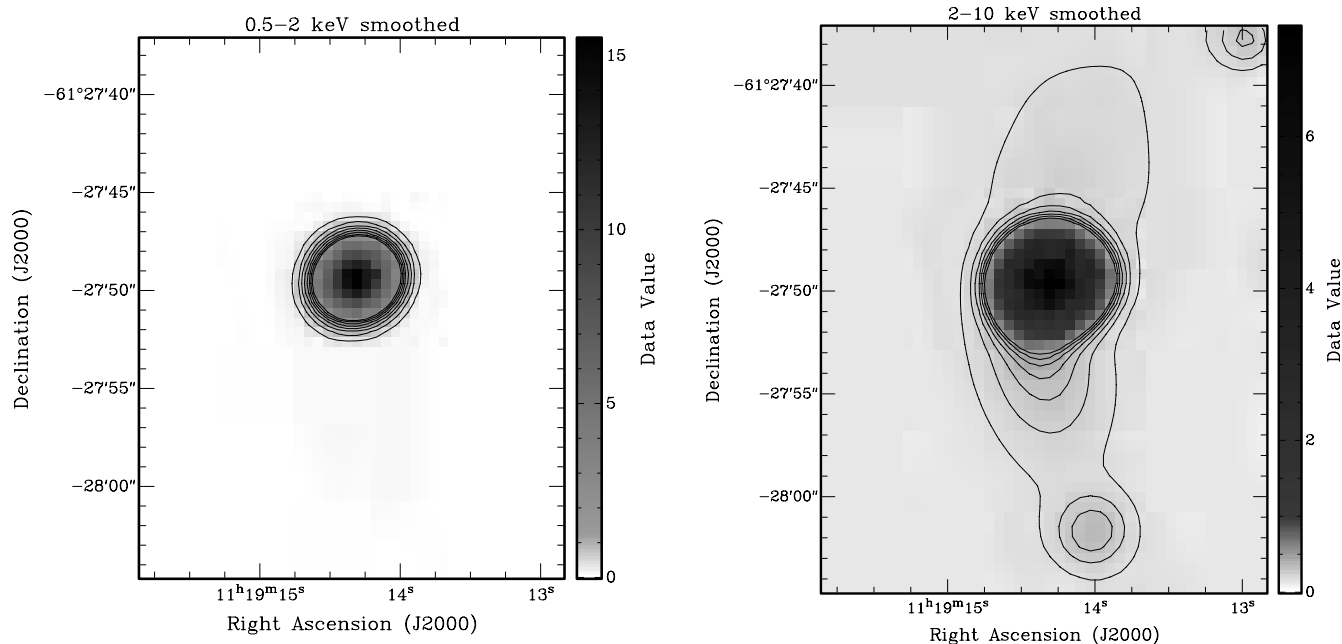


FIG. 4.— Same images as in Fig. 3, adaptively smoothed (with *csmooth*) using a Gaussian with $\sigma = 1''$ for a significance of detection greater than 5 and up to $\sigma = 3''$ for a significance of detection down to 2. The PWN and its elongated morphology in the north-south direction is evident in the hard band image. Contours are overlaid on a linear scale, chosen to highlight the emission from the jets, and ranging from 2.5 to 17 counts pixel^{-1} in steps of 2 for the soft band image, and from 2.5 to 7 counts pixel^{-1} in steps of 0.75 for the hard band image.

0.5–7.0 keV band, as the spectra provided little useful information outside this range. The pulsar’s spectrum was grouped with a minimum of 20 counts bin^{-1} , while the PWN’s spectrum was binned using a minimum of 10 counts bin^{-1} . Errors are at the 90% confidence level throughout the paper.

4.1. PSR J1119–6127

The spectrum of PSR J1119–6127 was extracted using a circle centered at the position of the pulsar (§ 3) and with a radius

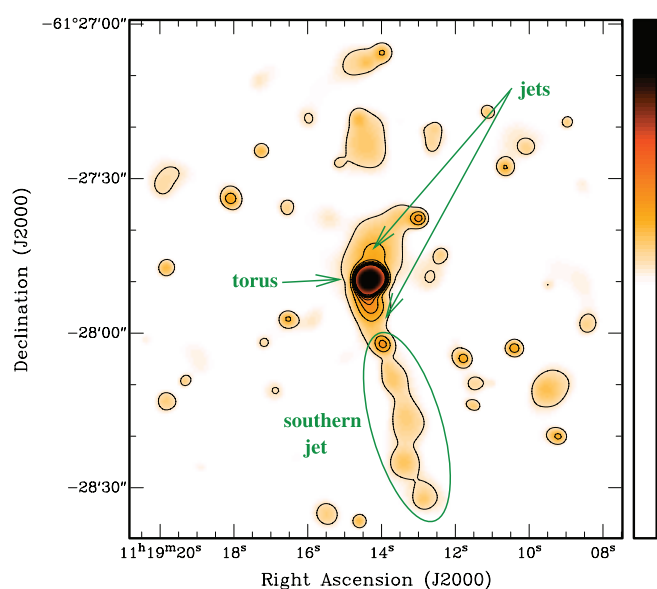


FIG. 5.— The 2–10 keV image of PSR J1119–6127 displaying the extended jet-like feature southwest of the pulsar. The image has been background-subtracted and smoothed as the previous figure. The overlaid contours range from 1.4 to 10 counts pixel^{-1} in steps of 1 in linear scale and are chosen to highlight the structure of the elongated jet.

of $2.5''$, thus encompassing 90% of the encircled energy.⁹ The background was extracted from a ring centered at the pulsar, extending from $3''$ to $4''$. This has the advantage of minimizing contamination by the PWN. We note, however, that the PWN contamination is negligible as its surface brightness is nearly 2 orders of magnitude smaller than the pulsar’s, and so the spectral results are practically independent of the background subtraction region (see, e.g., Safi-Harb [2008] for a preliminary analysis of the pulsar’s spectrum using a source-free background region taken from the S3 chip).¹⁰ The background-subtracted pulsar count rate is $(5.2 \pm 0.3) \times 10^{-3}$ counts s^{-1} for the 2833 observation, $(5.8 \pm 0.3) \times 10^{-3}$ counts s^{-1} for the 4676 observation, and $(3.7 \pm 0.5) \times 10^{-3}$ counts s^{-1} for the 6153 observation, thus accumulating $\sim 715 \pm 27$ total counts from the pulsar. To model the emission from the pulsar, we used a blackbody model to account for any surface thermal emission from the neutron star and a power law to account for any magnetospheric emission. A power-law model yields a column density $N_H = (1.2^{+0.4}_{-0.3}) \times 10^{22} \text{ cm}^{-2}$, a steep photon index $\Gamma = 3.0 \pm 0.5$, and an unabsorbed flux of $(1.7^{+1.3}_{-0.7}) \times 10^{-13} \text{ ergs cm}^{-2} \text{ s}^{-1}$, with a reduced χ^2 value $\chi^2_\nu = 1.356$ ($\nu = 31$ dof). A blackbody model does not yield an acceptable fit ($\chi^2_\nu = 2.166$, $\nu = 31$ dof), and as shown in Figure 6, it does not account for the emission above ~ 3 keV. Adding a power-law component to the blackbody model improves the fit significantly and yields an excellent fit with the following parameters: $N_H = (1.8^{+1.5}_{-0.6}) \times 10^{22} \text{ cm}^{-2}$, $\Gamma = 1.9^{+1.1}_{-0.9}$, $kT = 0.21 \pm 0.01 \text{ keV}$, and $\chi^2_\nu = 0.948$ ($\nu = 29$ dof), with the luminosity of the power-law component representing $\sim 30\%$ of the luminosity of the blackbody component (or $\sim 23\%$ of the total pulsar’s luminosity) in the 0.5–7.0 keV range. Figure 7 shows the blackbody+power-law model fit, and Table 1 summarizes the best-fit parameters.

⁹ See <http://cxc.harvard.edu/proposer/POG/html/ACIS.html>.

¹⁰ The tabulated values in Safi-Harb (2008) correspond to binning the data with a minimum of 10 counts bin^{-1} , whereas the data here are binned by a minimum of 20 counts bin^{-1} .

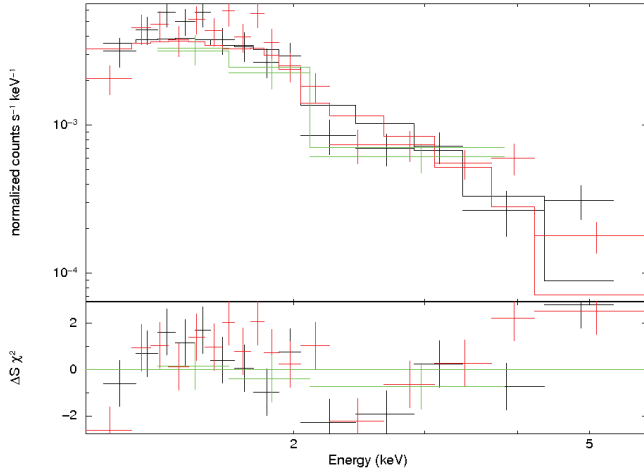


FIG. 6.—Spectrum of PSR J1119–6127 fitted with the blackbody model, illustrating the excess of emission above ~ 3 keV unaccounted for by the blackbody model. The lower panel shows the ratio of data to plotted model. The three colors refer to the three observations used in our analysis (ObsIDs 2833, *black*, 4676, *red*, and 6153, *green*).

The thermal and soft component is equally well fit with a neutron star magnetized ($B = 10^{13}$ G) atmospheric model (the NSA code in XSPEC; Zavlin et al. 1996). The parameters for the blackbody and atmospheric model are different, however, and as expected the NSA model yields a lower temperature than the blackbody model. Both models require a hard photon index ($\Gamma \sim 1.5$ – 2.0) for the power-law component. As shown in Table 1, the nonthermal unabsorbed flux amounts to $\sim 30\%$ – 35% of the thermal flux. In the NSA model, the distance was fixed to 8.4 kpc. We attempted to fit for this distance; however, we find that it is poorly constrained (ranging from 2.6 to 30 kpc). The best-fit parameters are $N_H = 1.6 \times 10^{22} \text{ cm}^{-2}$, $\Gamma_{\text{PL}} = 1.5$, $T_{\text{NSA}} = 1.6 \times 10^6 \text{ K}$, and $D = 8.4 \text{ kpc}$. Therefore, we restrict our discussion below to the fit with the fixed and reasonable distance of 8.4 kpc.

4.2. The PWN

The compact PWN’s spectrum was extracted from the elongated nebula ($\sim 6'' \times 15''$; see Fig. 4, *right*) with the pulsar region

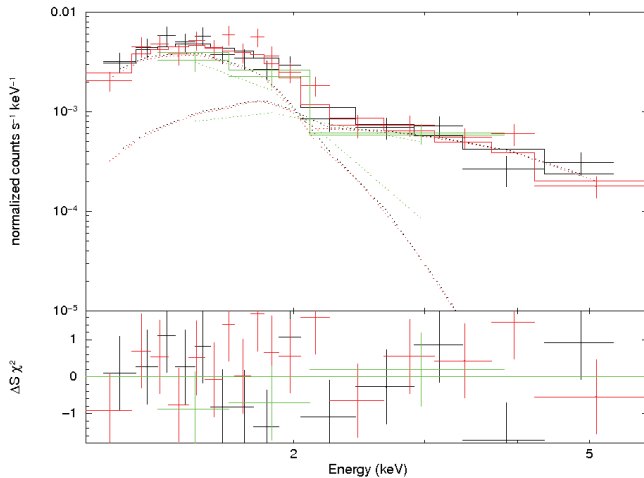


FIG. 7.—Spectrum of PSR J1119–6127 fitted with the BB+PL model shown in Table 1. The lower panel shows the ratio of data to plotted model. The dotted lines show the contributions of the blackbody (soft) and power-law (hard) components to the spectrum. The three colors refer to the three observations used in our analysis (ObsIDs 2833, *black*, 4676, *red*, and 6153, *green*).

TABLE 1
SPECTRAL FITS TO THE PULSAR

Parameter	PL	BB+PL	NSA+PL ^a
N_H (10^{22} cm^{-2}).....	$1.2^{+0.4}_{-0.3}$	$1.8^{+1.5}_{-0.6}$	1.6 ± 0.2
Γ	$3.0^{+0.5}_{-0.5}$	$1.9^{+1.1}_{-0.9}$	1.5 ± 0.8
Norm. ^b (PL).....	$5.7^{+4.2}_{-2.3} \times 10^{-5}$	$1.5^{+2.3}_{-0.9} \times 10^{-5}$	$8.4^{+1.5}_{-5.5} \times 10^{-6}$
kT_{eff} (keV).....	...	0.21 ± 0.01	$0.14^{+0.03}_{-0.02}$
Norm. ^b (BB).....	...	$3.5^{+1.5}_{-0.8} \times 10^{-6}$	1.42×10^{-8} (frozen)
$F_{\text{unabs}}^{\text{c}}$ (PL).....	$1.7^{+1.3}_{-0.7} \times 10^{-13}$	$6.7^{+0.7}_{-2.2} \times 10^{-14}$	$6.1^{+3.2}_{-1.9} \times 10^{-14}$
$F_{\text{unabs}}^{\text{c}}$ (thermal).....	...	$2.2^{+0.9}_{-0.5} \times 10^{-13}$	$1.8^{+1.9}_{-1.5} \times 10^{-13}$
L_X^{d} $10^{33} \text{ ergs s}^{-1}$	$1.4^{+1.1}_{-0.6}$	$2.4^{+0.8}_{-0.5}$	$2.1^{+0.8}_{-0.6}$
χ^2_{ν} (dof).....	1.356 (31)	0.948 (29)	0.977 (30)

NOTES.—All models are modified by interstellar absorption with a column density N_H . PL denotes a power-law model, BB denotes a blackbody, and NSA refers to the neutron star H atmospheric model in XSPEC version 12.4.0.

^a The NSA model assumes a magnetic field of 10^{13} G, a neutron star radius of 10 km, and mass of $1.4 M_{\odot}$. The distance is also fixed at 8.4 kpc (thus the normalization of 1.4×10^{-8}).

^b PL normalization at 1 keV in units of photons $\text{cm}^{-2} \text{ s}^{-1} \text{ keV}^{-1}$. BB normalization in units of L_{39}/D_{10}^2 where L_{39} is the luminosity in units of $10^{39} \text{ ergs s}^{-1}$ and D_{10} is the distance in units of 10 kpc.

^c 0.5–7.0 keV unabsorbed flux ($\text{ergs cm}^{-2} \text{ s}^{-1}$).

^d 0.5–7.0 keV total luminosity (assuming isotropic emission).

removed. The background was extracted from a nearby source-free region. The total number of background-subtracted counts accumulated from the PWN is only $\sim 103 \pm 17$ counts in the 0.5–7.0 keV range, therefore restricting our ability to constrain the spectral parameters or to perform a spatially resolved spectroscopy of the northern and southern extensions. However, fixing the column density to $1.8 \times 10^{22} \text{ cm}^{-2}$ (the best-fit value for the pulsar in the BB+PL fit; Table 1), we find that a power-law model yields a hard photon index $\Gamma = 1.1^{+0.9}_{-0.7}$, $\chi^2_{\nu} = 1.23$ ($\nu = 17$ dof), and a luminosity $L_X(0.5\text{--}7.0 \text{ keV}) \sim (1.6^{+2.3}_{-0.9}) \times 10^{32} d_{8.4}^2 \text{ ergs s}^{-1}$. Allowing N_H to vary $(1.2\text{--}3.3) \times 10^{22} \text{ cm}^{-2}$ (the range allowed by the PL+BB model fit to the pulsar), the PWN’s index is $\Gamma = 0.6\text{--}2.9$, typical of PWNs.

We subsequently extracted a spectrum from the southern jet (region shown in Fig. 5) and used the same background region as for the compact PWN. As mentioned earlier, we accumulated a total of $\sim 100 \pm 23$ source counts from this region in the 0.5–7.0 keV range, again too small to constrain the parameters or perform a spatially resolved spectroscopy along this feature. Fixing the column density to $1.8 \times 10^{22} \text{ cm}^{-2}$, the power-law model yields a photon index of $\Gamma = 1.4^{+0.8}_{-0.9}$, $\chi^2_{\nu} = 1.16$ ($\nu = 17$ dof), and a luminosity of $L_X(0.5\text{--}7.0 \text{ keV}) \sim (2.1^{+3.3}_{-1.2}) \times 10^{33} d_{8.4}^2 \text{ ergs s}^{-1}$. These values are not unusual for PWN structures. A thermal bremsstrahlung model is rejected on the basis of the unrealistically high temperature ($kT \geq 10 \text{ keV}$). Experimenting with two-component models was not possible, given the insufficient number of counts. In Table 2 we summarize the best-fit power-law model results.

5. DISCUSSION

5.1. The Pulsar

For the first time, we have resolved the pulsar’s spectrum and determined its properties independently of the PWN. We note here that the hard X-ray component in the *XMM-Newton* spectrum has been attributed entirely to the emission from the PWN (Gonzalez et al. 2005). We believe that this component is contaminated by the hard X-ray emission from the pulsar since *XMM-Newton*’s PSF does not allow the resolving of both components. In fact, an on-off pulse spectroscopic analysis of *XMM-Newton*’s

TABLE 2
POWER-LAW SPECTRAL FITS TO THE PWN

Parameter/PWN Region	Compact PWN	Southern Jet
Γ	$1.1^{+0.9}_{-0.7}$	$1.4^{+0.8}_{-0.9}$
Norm. ^a	$(2.2^{+2.8}_{-1.2}) \times 10^{-6}$	$(3.5^{+5.6}_{-1.9}) \times 10^{-6}$
χ^2_ν (dof)	1.23 (17)	1.16 (17)
f_{unabs} (0.5–7 keV) ergs cm ⁻² s ⁻¹	$(1.9^{+2.7}_{-1.0}) \times 10^{-14}$	$(2.5^{+3.9}_{-1.4}) \times 10^{-14}$

NOTES.—The compact PWN refers to the $6'' \times 15''$ structure elongated in the north-south direction (see Fig. 4). The southern jet corresponds to the new faint and extended jetlike structure ($\sim 6'' \times 20''$) shown in Fig. 5. N_H is frozen to 1.8×10^{22} cm⁻². Errors are 2σ .

^a Normalization at 1 keV in units of photons cm⁻² s⁻¹ keV⁻¹.

spectrum shows evidence of pulsed power-law emission at the 2σ level (M. Gonzalez 2008, private communication).

The single blackbody model is rejected (see § 4.1 and Fig. 6). As shown in Table 1, the best-fit model requires two components: a thermal component described by a BB or NSA model, and a power-law component with a photon index $\Gamma \sim 1.5$ – 2.0 . The column density is model-dependent. GSH03 derived an $N_H = (9^{+5}_{-3}) \times 10^{21}$ cm⁻² for the pulsar. Using *XMM-Newton*, Gonzalez et al. (2005) derived a higher N_H in the $(1.3$ – $2.7) \times 10^{22}$ cm⁻² range (depending on the model used). Our best-fit two-component models shown in Table 1, which adequately account for the hard (above 3 keV) emission, yield a column density of $(1.4$ – $1.8) \times 10^{22}$ cm⁻² in the NSA+PL model, and $(1.2$ – $3.3) \times 10^{22}$ cm⁻² in the PL+BB model. These ranges bracket the value derived using HEASARC's N_H tool¹¹ and overlap with the values derived previously with *Chandra* and *XMM-Newton*.

Using the thermal model in the two-component fits tabulated in Table 1, we now estimate the thermal properties of the pulsar. In the blackbody fit, the radius is inferred from equating the isotropic luminosity ($4\pi D^2 F$, where D is the distance to the pulsar and F is the unabsorbed flux, tabulated in Table 2) with the surface emission from the neutron star ($4\pi R^2 \sigma T_{\text{eff}}^4$, where σ is the Stefan Boltzmann constant), yielding $R = 2.7 \pm 0.7$ km, suggesting polar cap emission with a temperature of $T_{\text{eff}} = 0.21 \pm 0.01$ keV $= (2.46 \pm 0.12) \times 10^6$ K. The inferred radius is, however, larger than the conventional polar cap radius: $R_{\text{pc}}(\text{km}) \simeq 0.5(P/0.1 \text{ s})^{-1/2} = 0.25$ km (for $P = 408$ ms). The pulsar's thermal luminosity (assuming isotropic emission) is $L_X(0.5$ – $7.0 \text{ keV}) = (1.87^{+0.8}_{-0.4}) \times 10^{33} d_{8.4}^2$ ergs s⁻¹.

In the atmospheric (NSA) model, the temperature is $T_{\text{eff}} = (1.59^{+0.35}_{-0.23}) \times 10^6$ K, implying a temperature as seen by an observer of $T_{\text{eff}}^\infty = g_r T_{\text{eff}} = (1.22^{+0.27}_{-0.18}) \times 10^6$ K, where g_r is the redshift parameter given by $g_r = [1 - 2.952(M/R)]^{0.5} = 0.766$ for a neutron star of mass $M = 1.4 M_\odot$ and radius $R = 10$ km. The pulsar's bolometric luminosity as seen by an observer and assuming thermal emission from the entire neutron star's surface is $L_{\text{bol}}(0.5$ – $7.0 \text{ keV}) = g_r^2(4\pi R^2 \sigma T_{\text{eff}}^4) = (2.67 \pm 1.9) \times 10^{33} d_{8.4}^2$ ergs s⁻¹. These estimates differ from the values inferred by Gonzalez et al. (2005), mainly because the distance was fixed here at 8.4 kpc, while it was fit with *XMM-Newton*. Our values for both the blackbody and NSA model are, however, consistent with those derived independently by Zavlin (2007a).

The thermal emission from the pulsar was already discussed by Gonzalez et al. (2005) and Zavlin (2007a), who point out that the large pulsed fraction detected in the soft band is hard to interpret in either the blackbody or the NSA model (assuming

uniform surface emission). The large pulsed fraction indicates that the thermal emission is intrinsically anisotropic and that the effective temperature derived in the NSA model should be used as the mean surface temperature (Zavlin 2007b). We here point out to a puzzle related to the interpretation of the hard nonthermal pulsar emission, seen for the first time with the *Chandra* observations presented here. The nonthermal emission is presumably magnetospheric emission, as seen in other young active pulsars. Such an emission is expected to be pulsed. As mentioned earlier, *XMM-Newton* could not resolve the pulsar's emission from the PWN; however, an on-off pulse spectroscopic study of the *XMM-Newton* spectrum shows a hint of pulsed power-law emission from the pulsar. A long observation with *Chandra* in the timing mode and/or a deeper *XMM-Newton* observation will confirm and constrain the pulsed component in the hard band.

5.2. The PWN

The PWN is well described by a power-law model with a hard photon index ~ 1.1 for the compact PWN and ~ 1.4 for the southern extended jet (for a column density fixed at 1.8×10^{22} cm⁻²), and with a total X-ray luminosity of $\approx 4 \times 10^{32} d_{8.4}^2$ ergs s⁻¹ (0.5–7 keV). This represents $\lesssim 20\%$ of the pulsar's luminosity and $\lesssim 0.02\%$ of \dot{E} , implying an efficiency that is comparable to PSR B1800–21 and other Vela-like pulsars (Kargaltsev et al. 2007).

PWNs have been observed to have axisymmetric morphologies, including a toroidal structure and jets along the pulsar's spin axis. The emission from the torus is commonly attributed to synchrotron emission from the relativistic pulsar wind in the presence of a toroidal magnetic field in the equatorial plane and downstream of the shock. Jetlike structures, on the other hand, are attributed to magnetically collimated winds along the pulsar's rotation axis. The collimation and acceleration of the jets is strongly dependent on the pulsar's wind magnetization σ , defined as the ratio of electromagnetic to particle flux. At higher magnetization, equipartition is reached in the close vicinity of the termination shock, and most of the plasma is diverted and collimated into a jet along the polar axis. Therefore, the morphology of the PWN sheds light on the geometry of the pulsar and the intrinsic parameters of the pulsar wind (see, e.g., Gaensler & Slane 2006 and Bucciantini 2008 for reviews).

The jetlike structures seen north and south of PSR J1119–6127 could be interpreted as collimated outflows along the pulsar's polar axis, in which case a torus could be expected in the east-west direction. A torus-like structure is, however, barely resolved, and the PWN emission is mostly evident in the form of elongated jets (see Figs. 3–5), suggesting a high- σ wind. In the following, we use the spectral properties of the PWN to infer its intrinsic properties such as the termination shock, magnetic field, and σ .

The termination shock site (r_s) is estimated by equating the thrust of the pulsar, $\dot{E}/(4\pi r_s^2 c \Omega)$, with the pressure in the nebula, $P \approx B_n^2/4\pi$, where Ω is the pulsar's wind solid angle, which accounts for a nonisotropic wind, and B_n is the nebular magnetic field, which can be approximated from its equipartition value B_{eq} . To estimate B_{eq} , we use the nonthermal properties of the compact PWN (see Table 3) and assume the emission region to be a cylinder with radius $r_n \leq 3'' = 0.12 d_{8.4}$ pc and length of $l \sim 15'' = 0.61 d_{8.4}$ pc, resulting in an emitting volume of $V \sim 8.4 \times 10^{53} f d_{8.4}^3$ cm³, where f is the volume filling factor. Using a luminosity of $L_X(0.5$ – $7.0 \text{ keV}) \sim 2 \times 10^{32} d_{8.4}^2$ ergs s⁻¹ and assuming a ratio of 100 for the baryon to electron energy density, we estimate a magnetic field of $B_{\text{eq}} \geq 4.5 \times 10^{-5} (f d_{8.4})^{-2/7}$ G. The corresponding nebular pressure is $1.6 \times 10^{-10} (f d_{8.4})^{-4/7}$ ergs cm⁻³, and the termination shock is at a radius $r_s \sim 0.06 (f d_{8.4})^{2/7} \Omega^{-1/2}$ pc

¹¹ This tool calculates the weighted average measurement of the total Galactic column density toward the source's coordinates based on the Dickey & Lockman (1990) H I map.

TABLE 3
THE HIGH MAGNETIC FIELD PULSARS SORTED IN ORDER OF DECREASING SPIN-DOWN POWER

Pulsar (PSR)	\dot{E} (ergs s ⁻¹)	B (10 ¹³ G)	PWN?	$L_X(\text{psr} + \text{pwn})/\dot{E}$	Reference
J1846–0258.....	8.0×10^{36}	4.9	Y (X)	$0.018\text{--}0.0325^a d_6^2$	Kumar & Safi-Harb (2008)
J1119–6127.....	2.3×10^{36}	4.1	Y (X)	$5 \times 10^{-4} d_{8.4}^2$	This work
J1734–3333.....	5.6×10^{34}	5.2	Morris et al. (2002)
J1718–3718.....	1.5×10^{33}	7.4	...	$0.013\text{--}4.0 d_{4.5}^2$	Kaspi & McLaughlin (2005)
J1814–1744.....	4.7×10^{32}	5.5	...	$< 1340 d_{10}^2$ ^b	Pivovarov et al. (2000)
J1819–1458 ^c	2.9×10^{32}	5.0	...	$\sim 12 d_{3.6}^2$	Reynolds et al. (2006)
J1847–0130.....	1.7×10^{32}	9.4	...	$< 18\text{--}47 d_8^2$ ^d	McLaughlin et al. (2003)
B1800–21.....	2.2×10^{36}	0.4	Y(X)	$10^{-4} d_4^2$	Kargaltsev et al. (2007)
J1357–6429.....	3.1×10^{36}	0.8	Y(X)	$6.5 \times 10^{-5} d_{2.5}^2$	Zavlin (2007b)

NOTES.—We used the ATNF pulsar catalog in compiling the pulsar properties and only selected pulsars with $B \geq 4 \times 10^{13}$ G (the QED value) (B is defined in footnote 4, but see footnote 13). The last two pulsars, shown only for comparison with PSR J1119–6127, are rotation-powered pulsars with a typical magnetic field, but with \dot{E} and X-ray properties almost identical to PSR J1119–6127. The fourth column refers to the presence (Y) or absence of a PWN in X-rays (X). Except for PSR J1846–0258, none of these pulsars has a radio PWN associated with it. The fifth column refers to the ratio of the nonthermal X-ray luminosity of the combined pulsar and associated PWN (when detected in X-rays) to the pulsar's spin-down power, scaled to the distance given in units of d_x , where x is the adopted distance to the pulsar in units of kpc.

^a The lower (upper) range corresponds to the 2000 (2006) *Chandra* data; the pulsar has brightened by a factor of ~ 6 in 2006.

^b Only an upper limit on the X-ray luminosity was estimated using the spectral properties of 1E 2259+586 (an AXP) as a template.

^c Pulsar classified as a rotating radio transient; the X-ray luminosity of the pulsar is uncertain by an order of magnitude.

^d Only an upper limit was estimated using AXPs 4U0142+61 or 1E 2259+586 as templates.

(or $1.5''$ at 8.4 kpc), comparable to B1800–21 other PWNs (Kargaltsev et al. 2007).

We can further check the above estimate by using the thermal pressure from the interior of the remnant ($\sim 2n_e kT$) as the pressure confining the PWN. Using the kT and n_e values derived from our spectral fits to the SNR interior (to be presented in our follow-up SNR paper), we derive an SNR internal thermal pressure of $\sim 2.9 \times 10^{-9}$ ergs cm⁻³. The resulting shock radius is $r_s \sim 0.015$ pc, smaller than our estimate above, but consistent for $(fd_{8.4})^{2/7} \Omega^{-1/2} = 0.25$. At a distance of 8.4 kpc, a termination shock radius of 0.015–0.06 pc translates to a radius of $r_s = 0.4''\text{--}1.5'' d_{8.4}$, which explains the lack of resolvable wisplike structures as seen in other (nearby) PWNs.

Using the basic Kennel & Coroniti (1984) model developed for the Crab nebula, we can further infer a rough value for the magnetization parameter $\sigma \sim (r_s/r_n)^2 \sim 0.02\text{--}0.25$. This value is larger than that inferred for Crab-like PWNs (see, e.g., Petre et al. 2007) but supports the picture for strong collimation of jets. We caution, however, that this estimate should not be taken at face value and should only be considered as evidence of a highly magnetized wind, as it was inferred using the simple model of Kennel & Coroniti (1984), which assumes an isotropic energy flux in the wind. More recent calculations, however, show that if hoop stresses are at work in the mildly relativistic flow, jet collimation can occur in the post-shock region, and estimates of σ using the Kennel and Coroniti model can be overestimated (see, e.g., Bucciantini 2008 and references therein for a review).

The corresponding synchrotron lifetime of a photon with an energy of E (keV) is roughly $\tau_{\text{syn}} \approx 36 B_{-4}^{3/2} E^{1/2} d_{8.4}^{-3/7}$ yr, where B_{-4} is the nebular magnetic field in units of 10^{-4} G, yielding an average velocity for the high-energy electrons to reach the edge of the southern jet of $\sim 0.093 c B_{-4}^{-3/2} E^{-1/2} d_{8.4}^{3/7}$. This velocity is not unusual and is smaller than the typical shocked wind velocity of $\sim 0.3c$.

We interpreted the elongated structures to the north and south of the pulsar as jets that could be aligned with the rotation axis of the pulsar. The northern extension is shorter in length and is approximately twice as faint as the southern jet. Assuming that these elongated features represent an approaching (south) and receding (north) jet with similar intrinsic surface brightness and

outflow velocities, we can use relativistic Doppler boosting to account for the observed difference in brightness (Mirabel & Rodriguez 1999). For the observed brightness ratio of ~ 2 and an energy spectral index $-\alpha \sim 0.1\text{--}0.4$ (Table 2), assuming a continuous jet, we estimate a velocity $v \cos \theta \sim 0.14\text{--}0.16c$, where θ is the inclination angle of the flow axis with respect to our line of sight. Since $\cos \theta \leq 1$ for all inclination angles, this represents a lower limit for the intrinsic velocity of these features, a result that is consistent with our estimate of the average velocity above.

Elongated jets have been observed in other PWNs; for example, PSR B1509–58 powers a $4'$ long jet (6 pc at a distance of 5.2 kpc), and Vela powers a $100''$ long jet (0.14 pc at a distance of 300 pc). Furthermore, velocities of $> 0.2c$ have also been inferred from X-ray studies of these jets: $v_j > 0.2c$ for B1509–58 (Gaensler et al. 2002) and $v_j \sim (0.3\text{--}0.6)c$ for Vela (Kargaltsev et al. 2003).

5.3. Comparison of PSR J1119–6127 to Other Rotation-powered Pulsars and Magnetars

There are currently seven pulsars including PSR J1119–6127 with magnetar-strength fields ($B \geq B_c = 4.4 \times 10^{13}$ G; see Table 3), but which have not been identified as magnetars, except for PSR J1846–0258, which most recently revealed itself as a magnetar (Kumar & Safi-Harb 2008; Gavril et al. 2008). One would ask then whether all other pulsars belonging to this class should be related to magnetars (e.g., by being quiescent magnetars), or whether they represent a distinct population of rotation-powered pulsars. To address this open issue, we compare the known properties of PSR J1119–6127 to magnetars and to the classical rotation-powered pulsars:

1. Unlike magnetars (even in quiescence) and like the classical rotation-powered pulsars, PSR J1119–6127 and its PWN are powered by rotation (L_X is much smaller than its \dot{E}) and the pulsar powers a hard PWN. In addition, its infrared properties resemble the rotation-powered pulsars more than the magnetars (Mignani et al. 2007)—the latter are known to be more efficient IR emitters.

2. Like magnetars and some rotation-powered pulsars (see more below), J1119–6127 is described by a two-component (blackbody+power-law) model. PSR J1119–6127's thermal temperature ($kT \sim 0.21$ keV in the BB+PL model and 0.14 keV in the NSA+PL

model) is intermediate between that of magnetars ($kT_{\text{BB}} \sim 0.41\text{--}0.67$ keV; Woods & Thompson 2006) and that of the Vela-like, rotation-powered, pulsars with a thermal component dominating at energies $E \leq 2$ keV (see Zavlin 2007b, Fig. 5). The relatively high temperature of PSR J1119–6127 (in comparison with the rotation-powered pulsars) can be accounted for by a neutron star cooling model with proton superfluidity in its core and a neutron star mass of $\sim 1.5 M_{\odot}$ (see Zavlin 2007b, Fig. 5). Its photon index (1.0–2.9 in the BB+PL model and 0.7–2.3 in the NSA+PL model; see Table 1) appears relatively hard in comparison to that of most AXPs in quiescence (see Woods & Thompson 2006, Table 14.1) and consistent with that expected from the rotation-powered pulsars, but also similar to that of three spectrally hard magnetars in their quiescent state (SGR 1806–20, SGR 1900+14, and AXP 1E 1841–045 having PL indices of 2.0, 1.0–2.5, and 2.0, respectively; Woods & Thompson 2006).

3. PSR J1119–6127's X-ray properties are most similar to two young "Vela-like" pulsars with a similar \dot{E} : PSR B1800–21 and PSR J1357–6429, rotation-powered pulsars with a more "typical" magnetic field (see Table 3 and references therein). Most notably, both pulsars power compact and hard PWNs and display an L_X/\dot{E} value comparable to PSR J1119–6127's. Furthermore, like PSR J1119–6127, the spectrum of PSR J1357–6429 has a thermal component that dominates the total flux at energies below 2 keV ($\sim 72\%$ for PSR J1357–642 vs. $\sim 87\%$ for PSR J1119–6127) and is strongly pulsed, despite its lower B field. Such a high pulsed fraction ($\geq 50\%$ at $E \leq 2$ keV; Zavlin 2007b) could be explained by intrinsic anisotropy of the thermal emission formed in a magnetized neutron star atmosphere coupled with a strong nonuniformity of the surface temperature and magnetic field distributions (V. E. Zavlin 2008, private communication; Zavlin 2007b). Such an interpretation can also be applied to PSR J1119–6127 whose thermal spectrum is also well fitted with a neutron star atmospheric model (see Table 1 and § 5.1; V. E. Zavlin 2008, private communication; Zavlin 2007a).

4. Among the high-B pulsars, PSR J1119–6127 has spin properties (i.e., P , B) most similar to those of PSR J1846–0258 (the Kes 75 pulsar). Both pulsars are also now believed to be at about the same distance of ~ 6 kpc. However, PSR J1846–0258 is a non-thermal X-ray pulsar characterized by a hard power-law index¹² ($\Gamma \leq 2$) and is much more efficient at powering a bright PWN [$L_X/\dot{E}(\text{PWN}) \sim 2\%$; see Kumar & Safi-Harb 2008], so their X-ray properties are very different. Furthermore, PSR J1846–0258 has recently revealed itself as a magnetar since magnetar-like X-ray bursts were detected with *RXTE* and its spectrum softened as its

flux brightened by a factor of ~ 6 (Gavriil et al. 2008; Kumar & Safi-Harb 2008). PSR J1119–6127 appears to have a stable spectrum between 2002 (ObsID 2833) and 2004 (ObsID 4676) with a count rate of $\sim 5.5 \times 10^{-3}$ counts s^{-1} (§ 4.1). ObsID 6153 yields a smaller count rate for the pulsar ($\sim 70\%$ the average count rate) suggesting variability; however, if real, we believe that it is not significant within error, given that *a*) ObsID 6153 was relatively short and taken the day following ObsID 4676, and *b*) magnetar outbursts normally cause a much brighter enhancement in the X-ray flux. It is possible, however, that PSR J1119–6127 will one day reveal itself as a magnetar after an occasional burst driven by its high B field, just like PSR J1846–0258 recently did. Monitoring PSR J1119–6127 and the other high-B pulsars in the radio and X-ray bands are needed to address this possibility.

Given the close resemblance of PSR J1119–6127 to the other rotation-powered pulsars with typical B-fields and a similar \dot{E} , we conclude that the global X-ray properties of PSR J1119–6127 are not (at least not entirely) determined by the high B value,¹³ and that \dot{E} in particular, and likely the environment, which should confine the PWN and therefore would affect its morphology and brightness, play a significant role in determining its properties.

Whether PSR J1119–6127 is a quiescent magnetar that is currently mainly powered by its \dot{E} , but that will one day reveal a magnetar-like identity, remains to be seen.

Finally, our study further suggests that PSR J1119–6127 is characterized by a highly magnetized wind, possibly explaining the evidence for a small torus and prominent jets. The deep search for X-ray emission and PWNs around the other high- B pulsars is warranted to address the question whether these pulsars are similarly characterized by highly magnetized winds. Given the small \dot{E} of most known high-B pulsars (Table 3), very long exposures will be needed to be sensitive to PWNs of luminosity $\approx 10^{-4}$ to $10^{-3} \dot{E}$.

S. S.-H. acknowledges support by the Natural Sciences and Engineering Research Council of Canada (NSERC) and the Canada Research Chairs program. This research made use of NASA's Astrophysics Data System, the High-Energy Astrophysics Science Archive Center operated by NASA's Goddard Space Flight Center, and the ATNF pulsar database.¹⁴ We thank the anonymous referee and F. Camilo for a detailed reading of the manuscript and for useful comments.

¹² We note here that the column density toward PSR J1846–0258 is at least twice as high as that toward PSR J1119–6127, thus possibly hindering the significant detection of any soft blackbody component (Kumar & Safi-Harb 2008).

¹³ One should also keep in mind that the actual magnetic field strength can be a factor of a few off from the spin-down value, and so pulsars with comparable B may have substantially different actual fields (see Camilo 2008 and references therein).

¹⁴ See <http://www.atnf.csiro.au/research/pulsar/psrcat/>.

REFERENCES

- Bucciantini, N. 2008, *Adv. Space Res.*, 41, 491
 Camilo, F. 2008, *Nature Physics*, 4, 353
 Camilo, F., Ransom, S. M., Halpern, J. P., & Reynolds, J. 2007, *ApJ*, 666, L93
 Camilo, F., Ransom, S. M., Halpern, J. P., Reynolds, J., Helfand, D. J., Zimmerman, N., & Sarkissian, J. 2006, *Nature*, 442, 892
 Camilo, F., et al. 2000, *ApJ*, 541, 367
 Caswell, J. L., McClure-Griffiths, N. M., & Cheung, M. C. M. 2004, *MNRAS*, 352, 1405
 Cordes, J. M., & Lazio, T. J. W. 2002, preprint (arXiv:0207156)
 Crawford, F., et al. 2001, *ApJ*, 554, 152
 Dickey, J. M., & Lockman, F. J. 1990, *ARA&A*, 28, 215
 Ebeling, H., White, D. A., & Rangarajan, F. V. N. 2006, *MNRAS*, 368, 65
 Gaensler, B. M., & Slane, P. O. 2006, *ARA&A*, 44, 17
 Gaensler, B. M., et al. 2002, *ApJ*, 569, 878
 Gavriil, F. P., Gonzalez, M. E., Gotthelf, E. V., Kaspi, V. M., Livingstone, M. A., & Woods, P. M. 2008, *Science*, 319, 1802
 Gonzalez, M. E., Kaspi, V. M., Camilo, F., Gaensler, B. M., & Pivovarov, M. J. 2005, *ApJ*, 630, 489
 Gonzalez, M. E., & Safi-Harb, S. 2003, *ApJ*, 591, L143 (GSH03)
 ———. 2005, *ApJ*, 619, 856
 Halpern, J. P., Gotthelf, E. V., Becker, R. H., Helfand, D. J., & White, R. L. 2005, *ApJ*, 632, L29
 Kargaltsev, O., Pavlov, G. G., & Garmire, G. P. 2007, *ApJ*, 660, 1413
 Kargaltsev, O. Y., Pavlov, G. G., Teter, M. A., & Sanwal, D. 2003, *NewA Rev.*, 47, 487
 Kaspi, V. M., & McLaughlin, M. A. 2005, *ApJ*, 618, L41
 Kennel, C. F., & Coroniti, F. V. 1984, *ApJ*, 283, 694
 Kumar, H. S., & Safi-Harb, S. 2008, *ApJ*, 678, L43
 McLaughlin, M. A., et al. 2003, *ApJ*, 591, L135

- Mignani, R. P., et al. 2007, *A&A*, 471, 265
- Mirabel, I. F., & Rodriguez, L. F. 1999, *ARA&A*, 37, 409
- Morris, D. J., et al. 2002, *MNRAS*, 335, 275
- Petre, R., Hwang, U., Holt, S. S., Safi-Harb, S., & Williams, R. M. 2007, *ApJ*, 662, 988
- Pivovarov, M. J., Kaspi, V. M., & Camilo, F. 2000, *ApJ*, 535, 379
- Pivovarov, M. J., Kaspi, V. M., Camilo, F., Gaensler, B. M., & Crawford, F. 2001, *ApJ*, 554, 161
- Reynolds, S. P., et al. 2006, *ApJ*, 639, L71
- Safi-Harb, S. 2008, in *AIP Conf. Proc.* 983, 40 Years of Pulsars, Millisecond Pulsars, Magnetars and More. pp. 213
- Slane, P. O., Helfand, D. J., & Murray, S. S. 2002, *ApJ*, 571, L45
- Woods, P., & Thompson, C. 2006, in *Compact stellar X-ray sources*. Eds. W. Lewin & M. van der Klis. *Cambridge Astrophysics Series*, No. 39. (Cambridge: Cambridge Univ. Press), 547
- Zavlin, V. E. 2007a, preprint (arXiv:0702426)
- . 2007b, *ApJ*, 665, L143
- Zavlin, V. E., Pavlov, G. G., & Shibano, Y. A. 1996, *A&A*, 315, 141